https://doi.org/10.5194/essd-2026-197
Preprint. Discussion started: 25 June 2026

Open Access Earth System Science Data Discussions

Flume experimental data for the study of morphological response of alpine gravel-bed rivers to flow and sediment forcing

Adèle Johannot*[1], Alain Recking*[1], Arthur Lopez[1], Hervé Bellot[1], Alexis Buffet[1], Firmin Fontaine[1], Kylian Bardot[2]

[1] National Institut of Geosciences IGE, INRAE, France
[2] Rocca E Terra, GEOTECH, France

Correspondence to: Adèle Johannot (ajohannot@gmail.com) and Alain Recking (alain.recking@inrae.fr)

Abstract. This paper presents a dataset derived from flume experiments designed to reproduce conditions typical of alpine gravel-bed streams. The experiments aim to investigate how different hydro-sedimentary forcings influence channel morphology. The flume setup is Froude-scaled based on measurements collected on a braided reach in the French Alps. Experimental runs represent daily flood peaks characteristic of the melting season, together with their associated sediment supply. The dataset includes several types of measurements: full-flume topography obtained by photogrammetry, bedload flux at the outlet measured with a force sensor, grain-size distribution of transported sediments, and flow surface velocities derived from a tracer method. Digital Elevation Models (DEMs) were generated from the photogrammetric surveys at multiple timesteps, with a spatial resolution of 0.7 mm/pixel and a mean vertical error of 1 mm. Bedload flux at the outlet can be estimated from the force sensor measurements, while the grain-size distribution of transported material was determined by sieving. For each run, the dataset includes a video of the run, DEMs of the bed at different timesteps, a video for flow velocities estimates, sediment flux and transported grain-size at the outlet, and the input liquid and solid discharges. This large dataset available at https://doi.org/10.57745/QM4ZOO comprises 115 DEMs, 35 videos for velocities estimates, 81 transported grain size distribution and videos for various input conditions. It offers strong potential for studying morphological processes at micro- to macro-scales and across various timescales, and a fabulous playground for numerical investigations.

Dataset details

The data are classified by different upstream configuration UCx, for which we ran different cycle of floods Cy, in which there are different type of flood FT. Each flood represents a 24h-flood in the field and last 4h at the flume scale. A 4h-flood is named a run.

https://doi.org/10.5194/essd-2026-197
Preprint. Discussion started: 25 June 2026

For each run, we obtained:

- Liquid and solid discharge at the input
- The topography of the flume
- Local flow videos with tracers
- Timelapse photos from top and full view
- Mass, grain size distribution, and data to estimate instantaneous bedload flux at the output

The file names are at least composed of (i) the upstream condition number UCx, with x=[1,2,3]; (ii) the cycle number y; (iii) the flood type (FT), LF or SF for large and small flood; (iv) the ID of the run z, ranging between 01 and 34. For the concerned files, there is additionally (v) the frequency of the measurement Hi (or Hi_Qi for UC1_C2). In that way, each file names have the same root written in the form UCx_Cy_FT_z_ending or UCx_Cy_FT_z_Hi_ending.

Table 1: Presentation of the file names.

Format	File Name root	File name ending	Number of file
.tiff	UCx_Cy_FT_z_Hi_ending	DEM	115
.mov	UCx_Cy_FT_z_ending	LSPIVk, k in [1,3]	46
.tiff	UCx_Cy_FT_z_Hi_ending	ortho	110
.txt	UCx_Cy_FT_z_ending	-	34
.mp3	UCx_Cy_FT_z_ending	TopView or FullView	50

Additional metadata files provide complementary information:

- Metadata_DataAvailability: Summary tables describing the availability and quality of the different data.
- Metadata_DEM: DEM names and associated errors.
- Metadata_GCPcoordinates: x,y,z coordinates of the Ground Control Points usefull for LSPIV video treatment.
- Metadata_LSPIV: Ground Control Points associated to each LSPIV video and corresponding discharge during the measurement.
- Metadata_Msout_TransportedGSD: Grain-size distributions and weighted mass measured at the outlet for each run.

All these data are also concatenated in the Metadata.xlsx file.

https://doi.org/10.5194/essd-2026-197
Preprint. Discussion started: 25 June 2026

Open Access Earth System Science Data Discussions

A Python script used within Agisoft Metashape to automate the generation of Digital Elevation Models (DEMs) from the photogrammetric image datasets is also given in the dataset.

1. Introduction

The morphological response of gravel-bed rivers arises from complex interactions among sediment transport rates, local grain sorting, bed geometry, and hydraulic conditions. Our understanding of these processes remains limited, largely because it is difficult to obtain accurate and reliable measurements of both hydraulic and sedimentary forcings during periods of dynamic adjustment. This difficulty is especially pronounced in mountainous environments, where high hydraulic power and active morphodynamics make field data collection logistically demanding and costly in terms of time and manpower. To overcome these limitations, flume experiments have been widely used since the early twentieth century, beginning with the pioneering work of Gilbert (1914). Physical models, most commonly based on Froude similarity (Ashworth et al., 1994), allow the relevant forces to be scaled down while maintaining dynamic similarity. This approach makes it possible to control experimental input parameters and to isolate key controlling factors such as discharge, sediment size, slope, and channel morphology.

Early studies enabled researchers to investigate the unstable dynamics of bedload transport and provided datasets used to calibrate bedload equations. Some experiments focused on the morphology and dynamics of braided rivers composed of gravel and sand (P. Ashmore, 1982; P. E. Ashmore, 1988; P. Ashmore & Parker, 1983), whereas others contributed to improving our understanding of grain surface processes such as armoring and bedform migration (Bacchi et al., 2014; Gomez, 1983; Iseya & Ikeda, 1987; Jackson & Beschta, 1982; Parker, Dhamotharan, et al., 1982; Parker, Klingeman, et al., 1982; Parker & Klingeman, 1982; Recking et al., 2009). Many of these experiments relied on simplified conditions (such as constant discharge, constant sediment supply, or uniform sediment size) which do not fully capture the complexity of natural river systems (Leduc, 2013).). In alpine environments, however, channel morphology and bedload transport are strongly influenced by seasonal variations in both sediment supply and discharge (Misset et al., 2019, 2020). This led us to design new flume experiments under transient flow and sediment conditions.

In addition, many previous flume studies do not provide the types of measurements required for robust numerical validation (Williams et al., 2016). With the development of new imagery-based techniques, initially applied in field studies (Lane et al.,

https://doi.org/10.5194/essd-2026-197
Preprint. Discussion started: 25 June 2026

2000, 2003), experiments can now generate three-dimensional models of bed morphology with high spatial and temporal resolution. These methods can be applied to dry beds (Deng et al., 2025; Lane et al., 2001; Middleton, 2017; Peirce, 2017) and, more recently, to wetted beds (Vesipa et al., 2017). Such approaches provide new data sets to investigate river morphodynamics and also enable the mapping of surface grain-size distributions (Carbonari et al., 2021) with methods derived from the field (Carbonneau, 2005; Carbonneau et al., 2005; Ribet et al., 2024). In this study, we take advantage of these methods to design a flume experiment that provides detailed information on bed morphology under complex conditions, reproducing the characteristics of a typical alpine gravel-bed stream.

The experiment aimed to study a typical field situation characterized by (i) a transition between an unconfined and a confined section and (ii) variations in bedload transport and discharge throughout the melt season. We set up the Froude-scaled flume experiment based on an alpine gravel-bed river (the Severaisse River, in the French Alps), allowing control over both sediment and flow inputs. The scaling down from the prototype did not only concern the dimensions of the channel, the slope, and the grain size distribution, but also the hydrographs and sediment rating curve established from field measurements (using an Elwha sampler). We simulate two different hydrographs with corresponding sediment inputs and measure the resulting morphological response for different flow entrance representing the specific confined stream entrance into braided reach. Additionally, we measure surface velocities, bedload rate at the outlet and transported grain-size distribution. This paper first presents the flume design and protocols followed by a description of the measurement methods and data-processing techniques. For each measured item, the measurement method and quality assessment are provided. An example of how to use the dataset is presented before concluding.

2. Flume setup and protocol

2.1. River reach reference and physical model

The prototype used for this study is the Severaisse river, which is an alluvial alpine stream having several braided reaches interconnected with confined channels (Figure 1a). Figure 1 presents the surveyed reach considered in this study.

https://doi.org/10.5194/essd-2026-197
Preprint. Discussion started: 25 June 2026

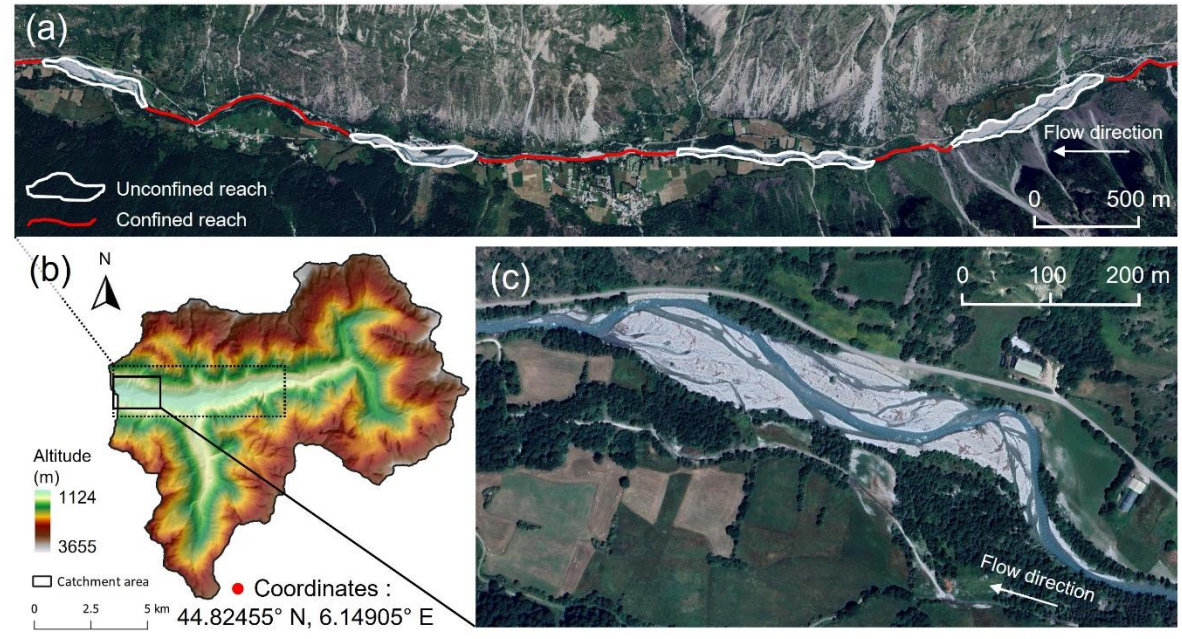

Figure 1: (a) Aerial views from the Séveraisse valley, showing the alternation of confined and unconfined reaches. (b) Catchment elevation and river location. (c) Aerial view of the reach where the data for flume sizing were obtained. Imagery © 2024 Airbus; Maps data © 2024 Google Earth.

The flume was scaled using Froude number similarity. Intensive field measurements presented by Recking et al. (2024) reported a mean slope of 1.6% and a mean 84th percentile of grain size distribution D_{84} of 108 mm. Our flume sediments have a D84 of 2.8mm, yielding a scaling ratio of 38.

Hydrology is influenced by snowmelt during spring and summer. A gauging station owned by the French Electricity Company measures discharge at the outlet of the reach (Figure 2a). Additionally, we performed direct bedload measurement during the melting season in 2018 and 2021 (Bakker et al., 2020; Nasr et al., 2023) to build a bedload rating curve (Figure 2b).

https://doi.org/10.5194/essd-2026-197
Preprint. Discussion started: 25 June 2026

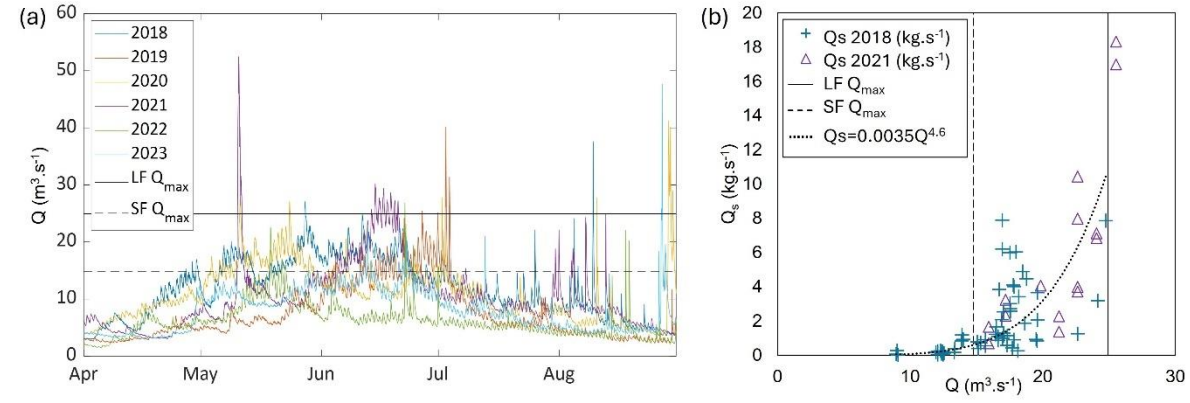

105 **Figure 2: (a) Snowmelt season hydrograph from 2018 to 2023. The full black line corresponds to the maximum peak of the flume run and the dotted line to the small flood peak run. (b) Bedload rating curve measured with an Elwha sampler in 2018 and 2021 snowmelt period.**

2.2. Experiment protocol and initial conditions

The experiment aimed at investigating: (i) the bed response at the transition between confined and unconfined reach and (ii) 110 at studying the influence of bedload and discharge variations through the melting season. Upstream, the water and sediments enter the flume through a coarse sediment fan to dissipate the energy of the waterfall. From this fan, we tested 3 different upstream conditions, representing different levels of constriction when the flow and sediment enter the flume. Figure 3 shows the different configuration referred to as UC1, UC2 and UC3 in the dataset.

115 **Figure 3: The different upstream inflow configurations: (a) 12° (configuration 1), (b) 52° (configuration 2), and (c) 0° (configuration 3).**

Multi-year field observations (morphodynamic changes) and measurements of bedload transport during snowmelt season (Misset et al., 2020; Recking et al., 2024) led us to conclude that the braided section is fed by upstream sediments only during

https://doi.org/10.5194/essd-2026-197
Preprint. Discussion started: 25 June 2026

moderate to major floods, and that during the rest of the year, the river transports the stocks in place downstream by incision until they are completely depleted.

Consequently, two situations are considered and differ if sediment enters or not the braided reach: large floods transporting sediment from the upstream reach, and small floods that do not transport sediment from the upstream constrained reach. Based on the river reach hydrological data (Figure 2a), two hydrographs were designed for the flume experiments, both representing daily flood events with symmetrical shapes (Figure 4a and b).

The first hydrograph corresponds to the mean maximum discharge ($25m^3.s^{-1}$ in the Séveraisse corresponding to $2.7L.s^{-1}$ in the flume) observed during snowmelt season over the past six years (the equivalent peak discharge is represented by the full black line in Figure 2). Inlet bedload flux at the flume entrance associated with this hydrograph was determined with the field bedload rating curve (Figure 2b). This hydrograph is referred to as 'LF', representing a large flood event (Figure 4a). The second hydrograph represents a smaller daily flood occurring at the end of the melting season (the equivalent peak discharge of $15m^3.s^{-1}$ is represented by the dotted black line in Figure 2). No inlet bedload flux was associated with this event, and it is referred to as the small flood 'SF' (Figure 4).

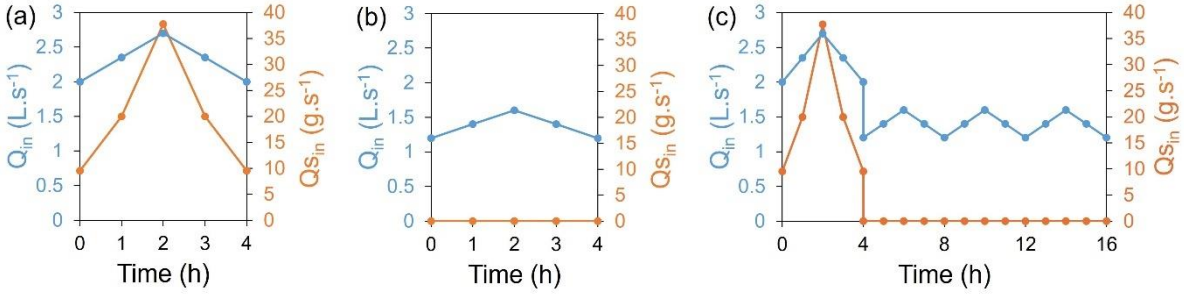

Figure 4 : (a) and (b) Hydrograph and associated sediment transport at the flume scale of the large flood event (LF) and the small flood event (SF), respectively. (c) Cycle represented by a large flood event followed by several small flood events.

From the latter hydrographs, we design a cycle of runs composed of one large flood event followed by several small events to represent the snow melt season period (Figure 4c). We ran this cycle for each upstream configuration at least twice, and seven time for UC3 (Table 2). Table 2 presents the total flood run associated to each upstream configuration, cycle and flood type. There is a total of 35 runs, composed of 11 large floods and 24 small floods.

https://doi.org/10.5194/essd-2026-197
Preprint. Discussion started: 25 June 2026

Open Access Earth System Science Data Discussions

Table 2: Run names for each flume configuration and each cycle.

Upstream configuration	Cycle	Flood run number				
		Large Flood	Small Flood			
UC1	1	01	02	03	04	05
	2	06	07	08		
UC2	1	09	10	11	12	
	2	13	14	15		
UC3	1	16	17	18		
	2	19	20	21	22	
	3	23	24	25		
	4	26	27	28		
	5	29	30			
	6	31	32			
	7	33	34	35		

The initial bed topography condition of each new run was the final topography of the last experiments. Doing so, we aimed at reproducing natural bed conditions without altering ongoing processes, like for instance, grain sorting.

Because the topography measurement was performed on a dry bed, each flood was artificially stopped every 1, 2 or 4h to perform the measurements. The hydrograph was divided per hour, noted Hi with i ranging from 1 to 4. We also did one cycle in UC1 with a higher stop frequency of every quarter, noted Qi with i ranging from 1 to 4. Because the speed of morphology changes is relatively low, we consider that these stops did not affect the bedload transport processes.

For each run, we measure:

- input liquid and solid discharges
- bed topography
- local flow videos with tracers
- timelapse photos from top and full view
- Sediment weight and grain size distribution at the output

2.3. Flume setup

https://doi.org/10.5194/essd-2026-197
Preprint. Discussion started: 25 June 2026

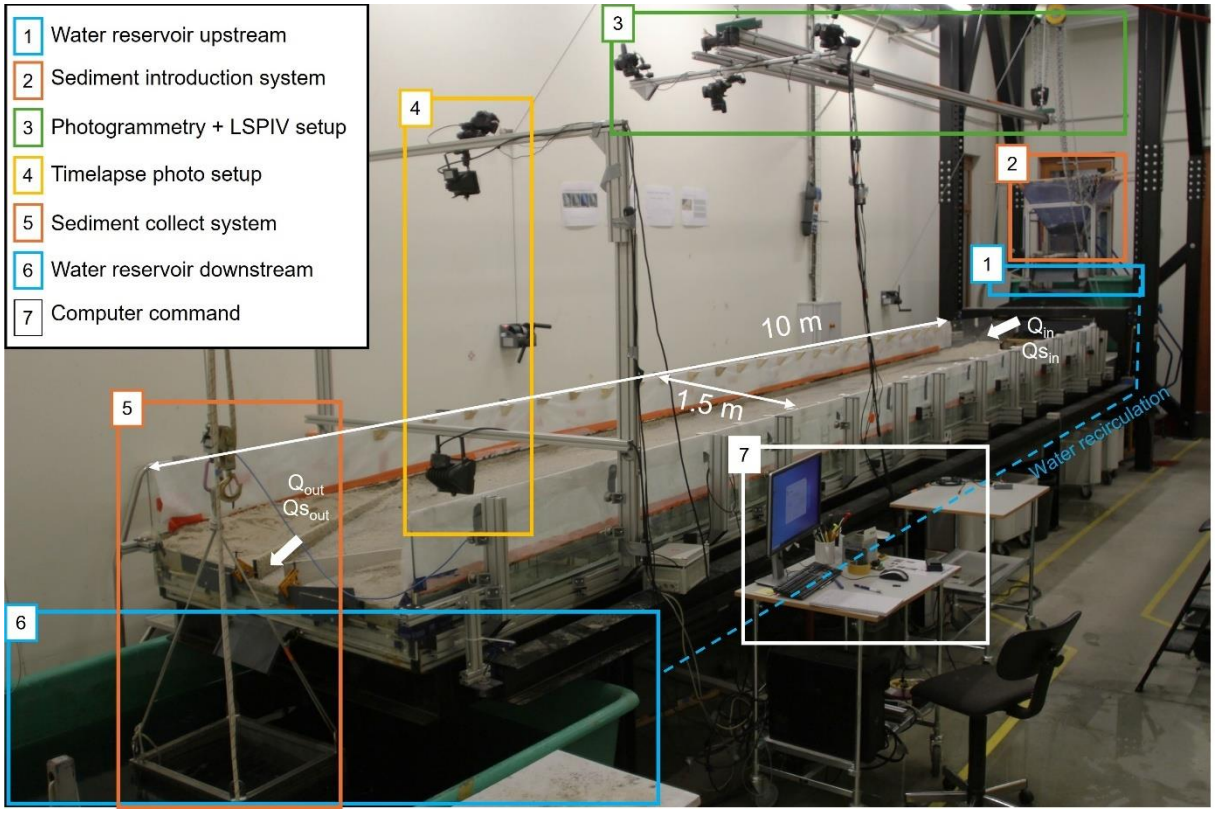

Figure 5: instrumentation used for data acquisition

The input water discharge Q_{in} and sediment discharge Qs_{in} are controlled by a computer system (items 1 and 2 in Figure 5). At the outlet, a sieved tank is used to separate and retain sediments before the water enters the reservoir (5 and 6 in Figure 5). For topography and surface velocities measurements, three cameras were mounted on a mobile trolley positioned above the flume (3 in Figure 5). An additional downstream camera was used for time-lapse recording to generate videos of each experimental run (4 in Figure 5).

https://doi.org/10.5194/essd-2026-197
Preprint. Discussion started: 25 June 2026

3. Data presentation

3.1. Liquid and solid discharge at the inlet

3.1.1. Control and measurement

The discharge, noted Q_{in}, is recirculated with a pump from the downstream to the upstream tank. From the upstream tank water is overflown through dissipative zone composed of cobbles, and located at the flume entrance. It is continuously measured at a 1s timestep using an electromagnetic flowmeter.

The sediment are introduced at the flume entrance using a system controlled by a motorized conveyor belt connected to a sediment tank (Figure 6). The sediment is moistened continuously with a system of water drops located above the sediment tank, in order to fluidize the mixture and avoid any blockage during the transfer through the system. Also, water jets located beneath the conveyor belt avoid the grains sticking to it.

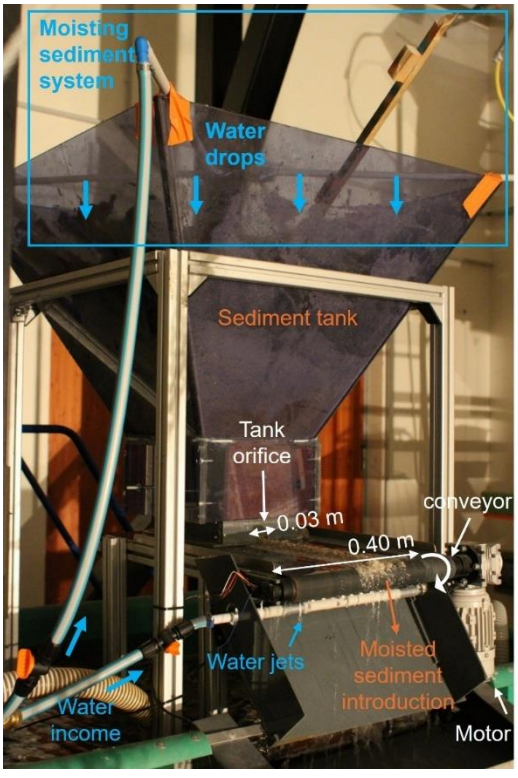

Figure 6: Sediment input system.

https://doi.org/10.5194/essd-2026-197
Preprint. Discussion started: 25 June 2026

A general calibration of the sediment feeding system was carried out by varying the belt velocity tension and by measuring the quantity of sediment evacuated per unit of time, given in Figure 7. Because the minimum sediment flux of the feeding system was relatively high, we had to reduce the time duration of sediment injection in order the reach the required mean Qs_{in} (see example in Figure 8b). This has no consequence on the real flux in the surveyed sections as the dissipation zone located at the flume entrance also acts as a buffer. The tension has been converted in sediment flux using the regression of Figure 7.

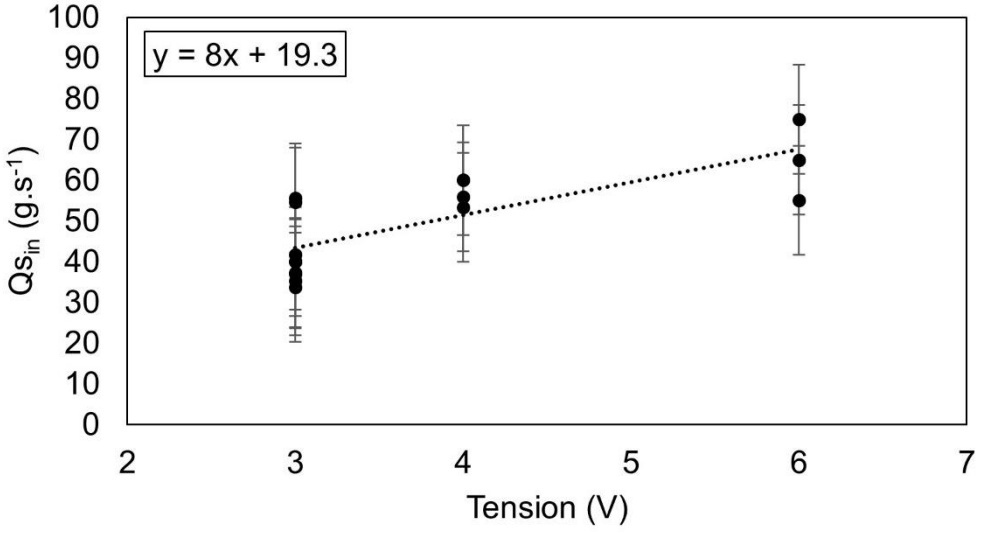

Figure 7: Calibration curve between the tension and the sediment flux at the inlet with measurement randomly performed during the run. The error bars represent the residual error related to the regression curve.

These data are available for each run in the .txt file in the Qin_Qsin_Qsout folder. Q_{in} corresponds to the third and fourth columns, representing the operated and measured discharge respectively (presented in Figure 8a). Qs_{in} is given in the fifth column.

https://doi.org/10.5194/essd-2026-197
Preprint. Discussion started: 25 June 2026

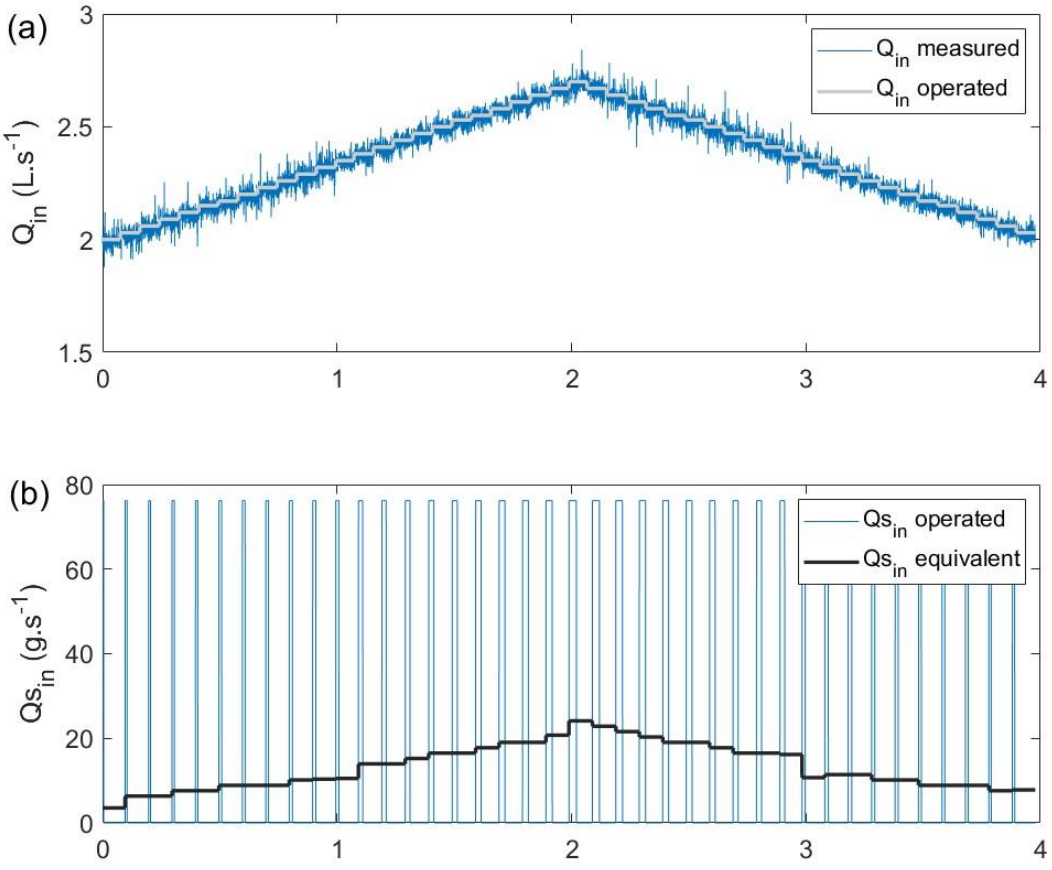

190 **Figure 8: (a) Inlet liquid discharge, with the** operated discharge **in** grey **and the** discharge measured by the **flowmeter in blue. (b) Inlet solid discharge, with the** discharhe operated **in blue and the equivalent mean discharge in** black**.**

3.1.2. Quality assessment

During the experiments, part of the flow infiltrates through the sediment bed. This subsurface or groundwater discharge was estimated by imposing a very low flow rate at the inlet and gradually increasing it until the water reached the thalweg of the
195 main channel without initiating surface flow. The magnitude of this discharge may vary depending on the morphological state of the bed, for example whether the channel is more or less incised. For this reason, the measurement was performed under the worst-case conditions, corresponding to a non-incised channel.

https://doi.org/10.5194/essd-2026-197
Preprint. Discussion started: 25 June 2026

In these conditions, the groundwater discharge Q_{gw} was estimated at 0.027 L.s^{-1}. Compared to the smallest discharge considered during the experiments (1.2 L.s^{-1}), it represents 2.2% of the total flow.

A small portion of the flow, which could not be quantified, was also lost through various leaks.

Additionally, water jets located beneath the conveyor belt avoid the grains sticking to it. This additional water supply Q_{jet} has been estimated at 0.047 L.s^{-1}, representing 4% of the minimum discharge (1.2 L.s^{-1}) and 1.7% for the maximum (2.7 L.s^{-1}). Hence, for LF floods for which water jets are used, discharge inside the channels can be corrected as following : Q_{in}-Q_{gw}+Q_{jet}= Q_{in}+0.02 L.s^{-1}. For SF, discharge inside the channels is Q_{in}-Q_{gw}= Q_{in}-0.027 L.s^{-1}.

The uncertainty in the sediment supply could not be quantified precisely. The sources of variability are numerous and include the degree of sediment moisture or the sediment load in the hopper at the time of the test. Unfortunately, we did not conduct a sufficient number of samples to rigorously account for this variability, but we estimated an indicator from 16 independent measurements. This uncertainty is estimated from the standard deviation of the regression residuals σ_{res}, computed with the 16 measurements. It reflects both the natural variability of sediment transport and instrumental uncertainties. It is defined by equation 1.

$$\sigma_{res} = \sqrt{\frac{1}{n-p}\sum(Qs_{in\ measured} - Qs_{in\ estimated})^2} \quad \textbf{(1)}$$

With $Qs_{in\ measured}$ the value of discharge flux presented in Figure 7, $Qs_{in\ estimated}$ the value estimated from the calibration curve presented in Figure 7, n the number of measurement and p the degree of freedom equal to 1 here. The final uncertainty with a 90% confidence interval is defined as $1.7\sigma_{res}$. Instantaneous measurements indicate that fluctuations can reach ± 13.4 g.s^{-1}. However, on average, despite these large fluctuations, this type of device can provide a steady mean sediment supply (Recking, 2006). To qualify better this variation, we calculated for each large flood the sediment mass injected by performing a sediment budget from the DEM using a sediment density of 2000kg/m^3 for wetted sands. We obtain a total mass varying between 126 to 194 kg (Table 1). We compared these values with the supposed injected mass calculated using the recorded data during the run and the calibration curve presented in Figure 7. The sediment budget mass fall within the uncertainty range of the calibration curve.

https://doi.org/10.5194/essd-2026-197
Preprint. Discussion started: 25 June 2026

Table 1: Calculation of sediment mass injected from the recorded data and calibration curve (referred to as Supposed injected mass) and from the sediment budget using the DEM (referred to as Sediment budget mass).

Large flood run	Tension (V)	Cumulated time of injection (s)	Qs_{in} ($g.s^{-1}$)	Supposed injected mass (kg)	Sediment budget mass (kg)
UC1_C1_LF_01	3	5094	43.3	220	Missing data
UC1_C2_LF_06	3	5531	43.3	239	158
UC2_C1_LF_09	3	5052	43.3	219	174
UC2_C2_LF_13	4	3828	51.3	196	193
UC3_C1_LF_16	6	2592	67.3	174	194
UC3_C2_LF_19	6	2388	67.3	171	127
UC3_C3_LF_23	6	2388	67.3	175	157
UC3_C4_LF_26	6	2388	67.3	175	143
UC3_C5_LF_29	6	2388	67.3	Missing data	Missing data
UC3_C6_LF_31	6	2388	67.3	188	Missing data
UC3_C7_LF_33	6	2388	67.3	195	167

3.2. Topography

3.2.1. Measurement

To quantify morphological changes, the Structure from Motion (SfM) method was adopted. This approach uses two-dimensional photographic images to reconstruct a three-dimensional representation of the surface, resulting in the generation of a Digital Elevation Model (DEM). Image processing was performed using Agisoft Metashape software, which is known to provide reliable results in both field and flume applications (Kingsland, 2020). The software was used to perform the standard photogrammetry workflow, which is described in detail below.

A key feature of this software is the use of control points, referred to as Ground Control Points (GCPs), positioned around the channel and whose coordinates are measured with a 1mm accuracy with a theodolite. The software automatically detects these points and uses them to align and scale the model to the real-world coordinates of the GCPs. It also provides an estimate of the systematic error, defined as the difference between the measured coordinates of the GCPs and the coordinates predicted by the reconstructed point cloud.

To achieve a high level of accuracy, particular attention must be paid to several aspects, including camera position, image quality, and the number and distribution of Ground Control Points (GCPs). Three cameras were used to capture the images.

https://doi.org/10.5194/essd-2026-197
Preprint. Discussion started: 25 June 2026

They are mounted on a mobile trolley suspended from the ceiling (see element 3 in **Figure 5**), allowing them to move along the channel. The two cameras located at the extremities have an oblique (radial) view in order to reduce dome effects during image alignment in Metashape (James et al., 2019; James & Robson, 2014). The central camera has a zenithal view, as it is also used to acquire timelapse photographs and LSPIV videos. Together, the three cameras provide a complete cross-sectional view of the channel, enabling targets positioned on both sides to be detected in all images (see example on Figure 9).

The mobile trolley is positioned at a height of approximately 2 m to allow easy access. The cameras are manually moved along the channel using a crank, stopping every 15 cm, which results in an overlap of approximately 85% between consecutive images. The open-source software DigiCamControl is used to trigger simultaneous image acquisition on all three cameras and to automatically download the photographs. In total, around 130 images are captured along the channel to generate a DEM.

Camera settings are crucial for image quality. It is preferable to use a camera with a long focal length to minimize edge distortion. Here, due to the height constraints of the rail, it was not possible to use cameras with focal lengths greater than 28 mm. The characteristics of each camera are as presented in table Table 2.

Table 2: Camera settings for photogrammetry.

Camera number	1	2	3
View type	radial	zenital	radial
Camera model	Canon EOS 1200D	Canon EOS 2000D	Canon EOS 1200D
Focal length (mm)	28	18	28
ISO	800	800	800
Exposure time ($.s^{-1}$)	1/60	1/60	1/60
Aperture	4	4	4
Image size (pixel)	3464x5202	6000x4000	3464x5202

Because the camera trolley was not long enough to cover the length of the flume, we had to add manual photos at both extremities with a fourth camera. This camera was the same model and had the same settings than the middle camera number 2. Upstream, only 5 photos were taken and downstream, a set of around 8 photos covering the following part.

https://doi.org/10.5194/essd-2026-197
Preprint. Discussion started: 25 June 2026

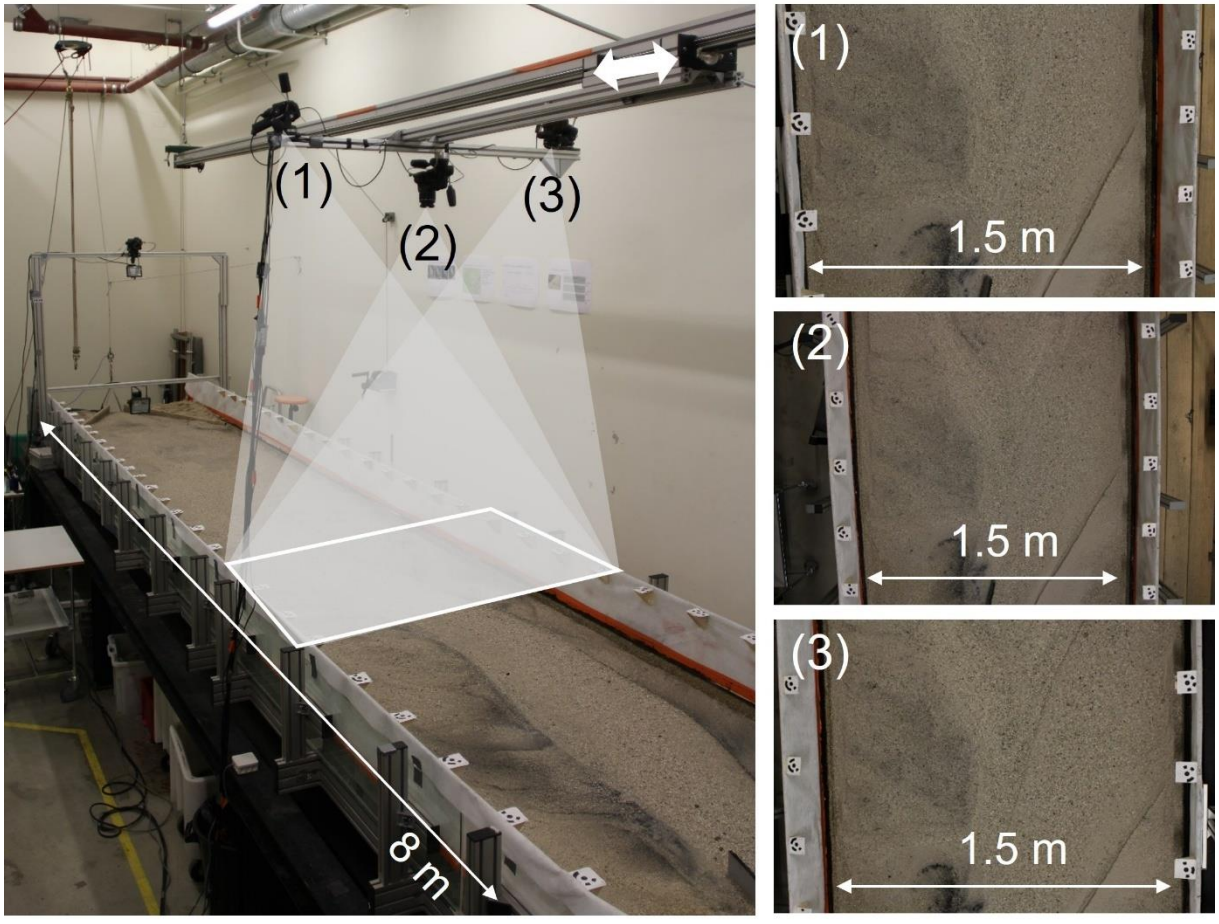

Figure 9: Photogrammetry acquisition.

3.2.2. Data processing and example

The program performs several processing steps to build a Digital Elevation Model (DEM) and is given in the dataset. The steps include:

- Photo alignment

Before beginning the alignment, we filter the bad quality photos using the quality estimation proposed by the software. We set a threshold at the value 0.7 based on visual appreciation and delete the photos beyond the threshold. Because of the extremity photos, we used an incremental mode for the alignment. For that, we first launch the alignment with the

https://doi.org/10.5194/essd-2026-197
Preprint. Discussion started: 25 June 2026

trolley photos, as it provides better quality than hand-taken extremity photos. Then, using the “reset camera alignment” function, we add the extremity photos and align them without resetting the previous alignment.

The alignment are performed with "ultra-high quality" because it provides a better quality of image. We set the key point limit to 1 000 000 and the tie point limit to 0, which mean that they are unlimited.

This alignment produces a point cloud of around 4 million points.

- Camera location optimization

The software automatically detects the targets and compares the real coordinates with the modeled ones in the 3 directions. GCPs are split in control points and check points. Control points are used for the optimization while the check points are used to estimate the error.

The optimization consists in reducing the errors between real coordinates of control points with their position in the point cloud. It reduces this error through optimizing camera location, with different coefficient while the wrong tie points are filtered. At the end of this step, the point cloud is corrected and the tie points filtered. For this optimization and tie point filtering, we used the recommended process provided by the USGS (United States Geological Survey) for coastal imagery (Over et al., 2021). We used the "Reconstruction uncertainty" filter with a targeted number for of 10 by allowing to remove less than 50% of tie points. The code iteratively computes the reconstruction uncertainty until it reaches the targeted value. When this value is reached, camera optimization is launched and the second filtering starts. We perform the "Projection accuracy" with a target value of 3. Finally, the "Reprojection error" is computed with a target number of 0.3. After the third camera optimization, the filtered and optimized point cloud counts approximately 700 000 points.

- Dense point cloud building

The point cloud needs to be densified before doing the digital elevation model. It was done by setting high quality and mild depth filtering, giving a final total point of 32 000 000 points.

- DEM and orthomosaic construction

https://doi.org/10.5194/essd-2026-197
Preprint. Discussion started: 25 June 2026

From the dense point cloud, a raster is constructed with a pixel size equal to the resolution of the camera, which is of 0.7mm, shown in Figure 10a. It also enables to generate orthomosaic, with a resolution of 0.355mm/pix, presented in Figure 10b.

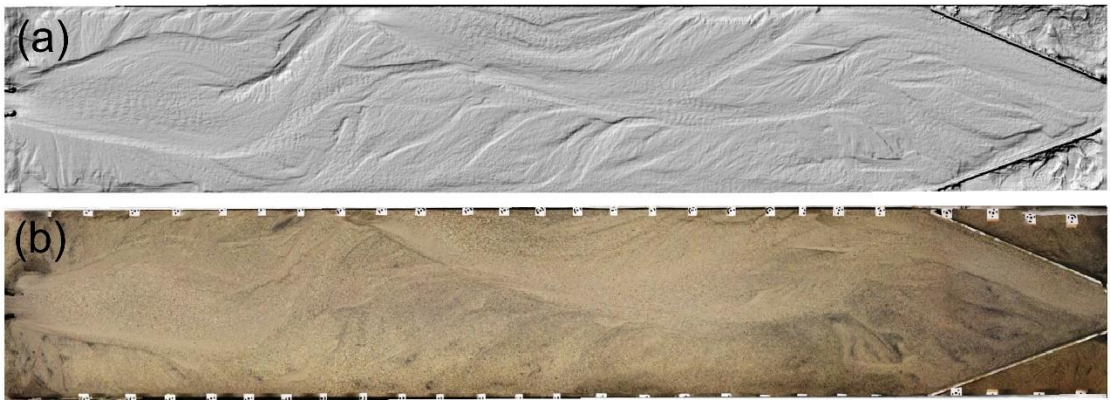

Figure 10: Example of a DEM (a) with associated orthomosaic (b).

3.2.3. Quality assessment

The final uncertainties that we consider for each DEM is the SDE (Standart Deviation Error) of the difference between check point GCPs real coordinates and the model, considered in the z and the xyz directions (equation 2, 3, 4).

$$SDE = \sqrt{\frac{1}{n-1}\sum_{i}(E_i - \frac{1}{n}\sum_{i}E_i)^2} \quad \textbf{(2)}$$

$$Ei,z = z_{meas} - z_{est} \quad \textbf{(3)}$$

$$Ei,xyz = \sqrt{(x_{meas} - x_{est})^2 + (y_{meas} - y_{est})^2 + (z_{meas} - z_{est})^2} \quad \textbf{(4)}$$

Where $(x_{meas}, y_{meas}, z_{meas})$ are the real coordinates measured with the theodolite and $(x_{est}, y_{est}, z_{est})$ are the coordinates estimated by Metashape and n the number of check points.

As the number of GCPs is important on the flume, we selected an equal number of check points and control points. The check points are equally spread on the flume, considering one on two and we thus consider that the SDE represents the overall error on most part of the flume, except the very upstream and downstream part. Indeed, because of the handmade photos of the

https://doi.org/10.5194/essd-2026-197
Preprint. Discussion started: 25 June 2026

extremities, the error is higher on those parts but we choose to exclude them from the optimization process to avoid that it affects the main part of the flume.

With this configuration, we obtain a mean SDE of 1mm in xyz, dans of 1.4mm in the vertical direction over the 115 DEMs. We calculated the SDE for each DEM which are given in the Metadata.xlsx file.

3.3. Surface flow velocities

3.3.1. Measurement

Charcoal was used as a tracer because it has been shown to provide satisfactory results (Piton et al., 2018) and does not affect either the sediments or the water in the flume. Data acquisition was performed using a Canon camera controlled via computer, recording at 50 frames per second. The camera was positioned to obtain a zenithal view, covering approximately 1.2 m of the flume length. A light diffuser was used to reduce water-surface reflections.

For each measurement, different areas of the flume were targeted in order to obtain representative observations. For efficient detection, the tracer should form surface striations that create distinctive patterns (see example in Figure 11b). However, due to local flow constrictions, it was sometimes impossible to produce such striations because tracer concentrations became too high at points of flow convergence.

There is, most of the time, one or more videos for each run. Discharge associated with each video is provided in the metadata file.

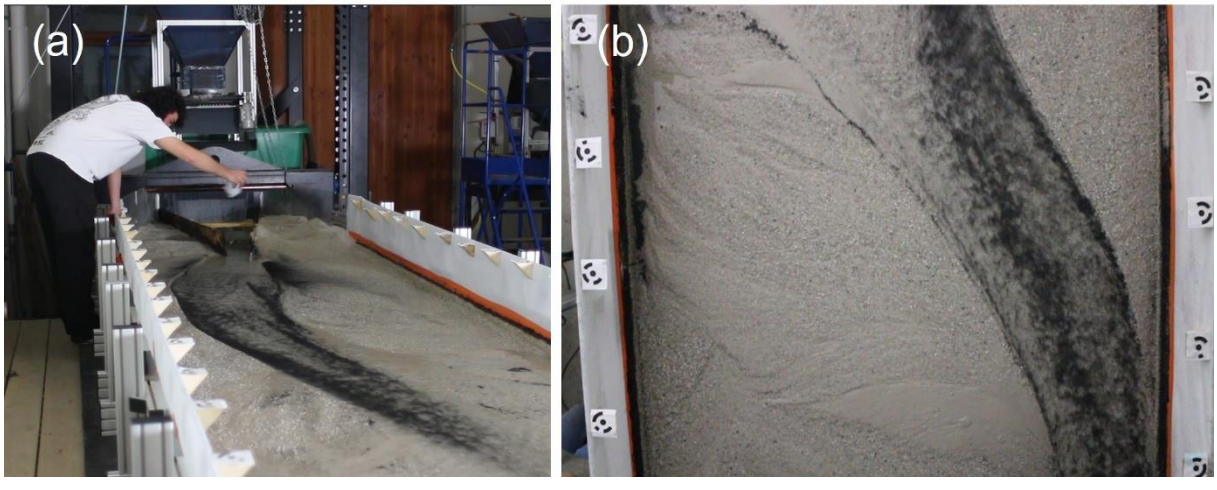

Figure 11: (a) Example of tracers spreading in the channel. (b) Top view as shown in the LSPIV videos.

https://doi.org/10.5194/essd-2026-197
Preprint. Discussion started: 25 June 2026

3.3.2. Potential treatment

These videos can be used to estimates field velocities. We recommend to use the software Fudaa-LSPIV developed by the French Electricity Company EDF, originally made for field but which is also suited for small scale (Hauet et al., 2014; Piton et al., 2018). It includes a phase of orthorectification of the images, which could be done using the GCPs coordinates. The GCP ID associated to each video is provided in the .xlsx file. They are ordered in the downstream direction, with GCP 1 to 24 in the right side and GCP 26 to 58 in the left side. GCP local coordinates measured with a theodolite with a precision of 1mm are provide in the 'GCP coordinates' sheet in the .xlsx file. An example of results is given in Figure 12.

However, due to the rather same altitude of the GCP, the orthorectification on Fudaa might be not correct and it is recommended to have points with different altitudes for better results. We recommend to add points targeted visually from which coordinates can be found with the DEM at the altitude of the flume bed for example.

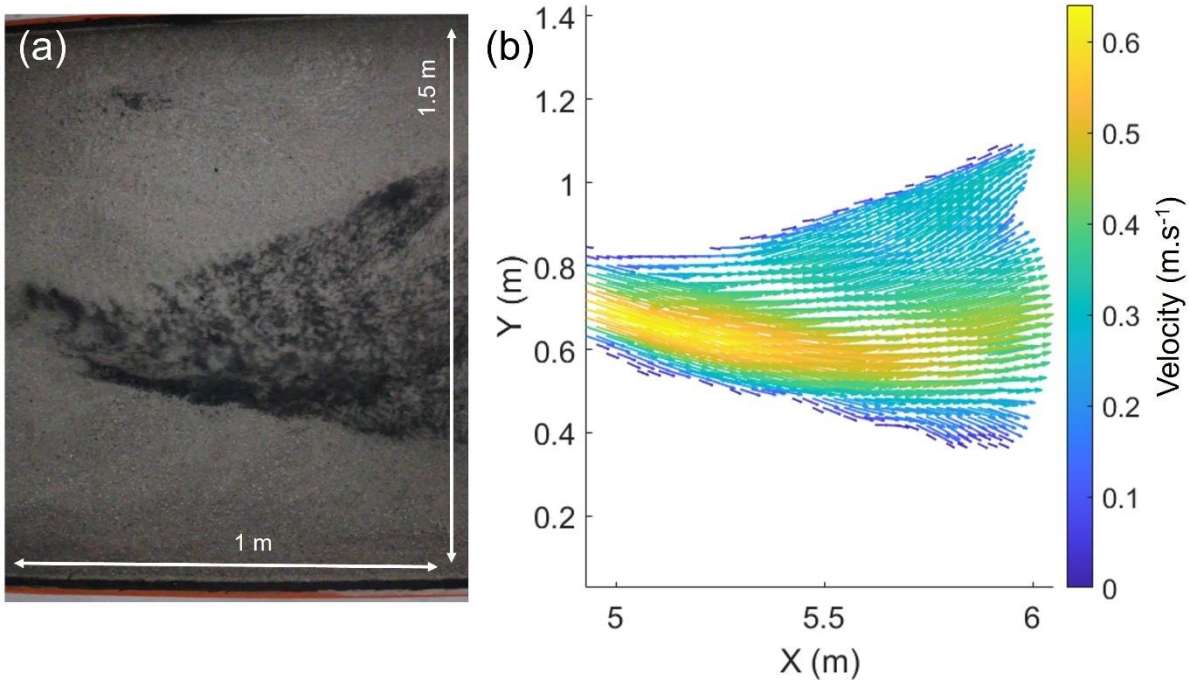

Figure 12: Example of flow velocity estimates. (a) Screenshot of the LSPIV video, before orthorectification. (b) Corresponding velocity estimates using the Fudaa software.

3.4. Timelapse video

https://doi.org/10.5194/essd-2026-197
Preprint. Discussion started: 25 June 2026

3.4.1. Measurement

Timelapse photos were performed to keep a visual evolution of the runs. We produced two videos for each run: one global view from downstream and a zoomed top view. For the global video, we used a camera at the outlet as shown in **Figure 5** with light spots to give a better contrast for the videos. At the same time, we used the middle camera 2 of the photogrammetry set-up to perform a zoomed video of the runs. The location of the top-view camera was mobile and we chose its position depending on the morphodynamics. The frequency of the timelapse was 60s.

3.4.2. Data processing

The final videos were created with a code. The associated discharge and sediment input are shown in the videos. Note that Q in the hydrograph corresponds to the measured discharge whereas Qs corresponds to the ideal sediment flux calculated from Q.

3.5. Sediment rate and grain size at the outlet

3.5.1. Measurement

A continuous solid discharge measurement system has been installed, using a force sensor carrying a sediment tank (Figure 13). The force sensor is suspended from the laboratory ceiling and attached to a filter box collecting the outgoing sediments while discharging the water. The force sensor measures a tension in V at 1s timestep (Figure 14a). This box is covered with a 0.1mm grid to capture the smallest sediments.

https://doi.org/10.5194/essd-2026-197
Preprint. Discussion started: 25 June 2026

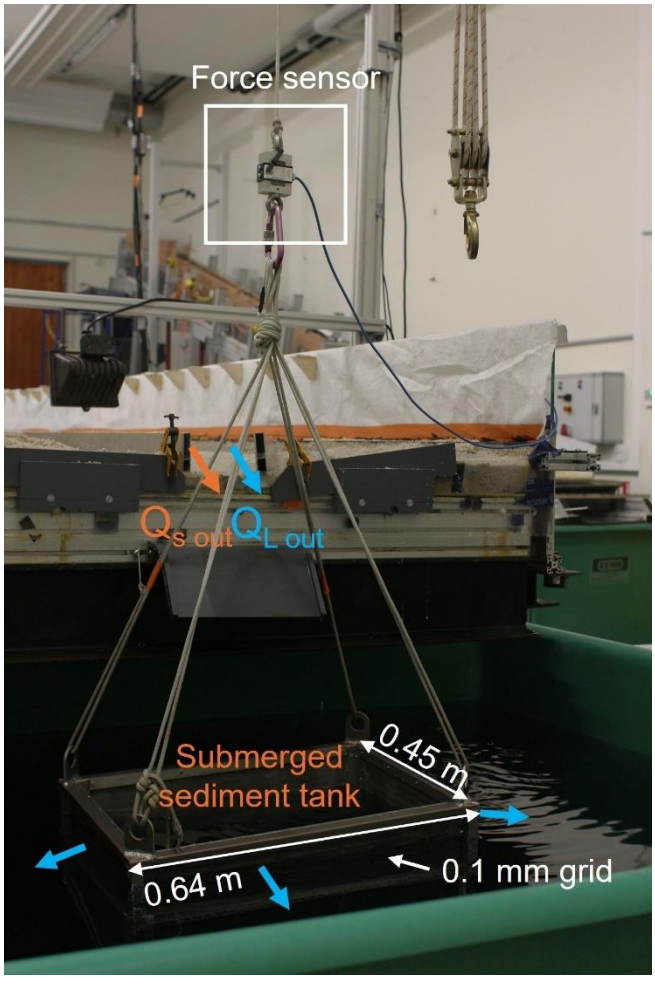

Figure 13: Sediment output measurement.

For each stop within the run, we measured the mass of dry sediment collected in the tank (Figure 14c), and we kept from it a random sample of around 300 to 1000g to do a sieving for grain size distribution (Figure 14d). We performed the grain size distribution measurement by sieving with 7 diameter class composed of 0.355, 0.71, 1, 1.4, 2, 2.8 and 5.6mm. The dry sediment mass and grain size distribution are given in the Metadata.xlsx file. An example of results obtained during a run is given in Figure 14.

https://doi.org/10.5194/essd-2026-197
Preprint. Discussion started: 25 June 2026

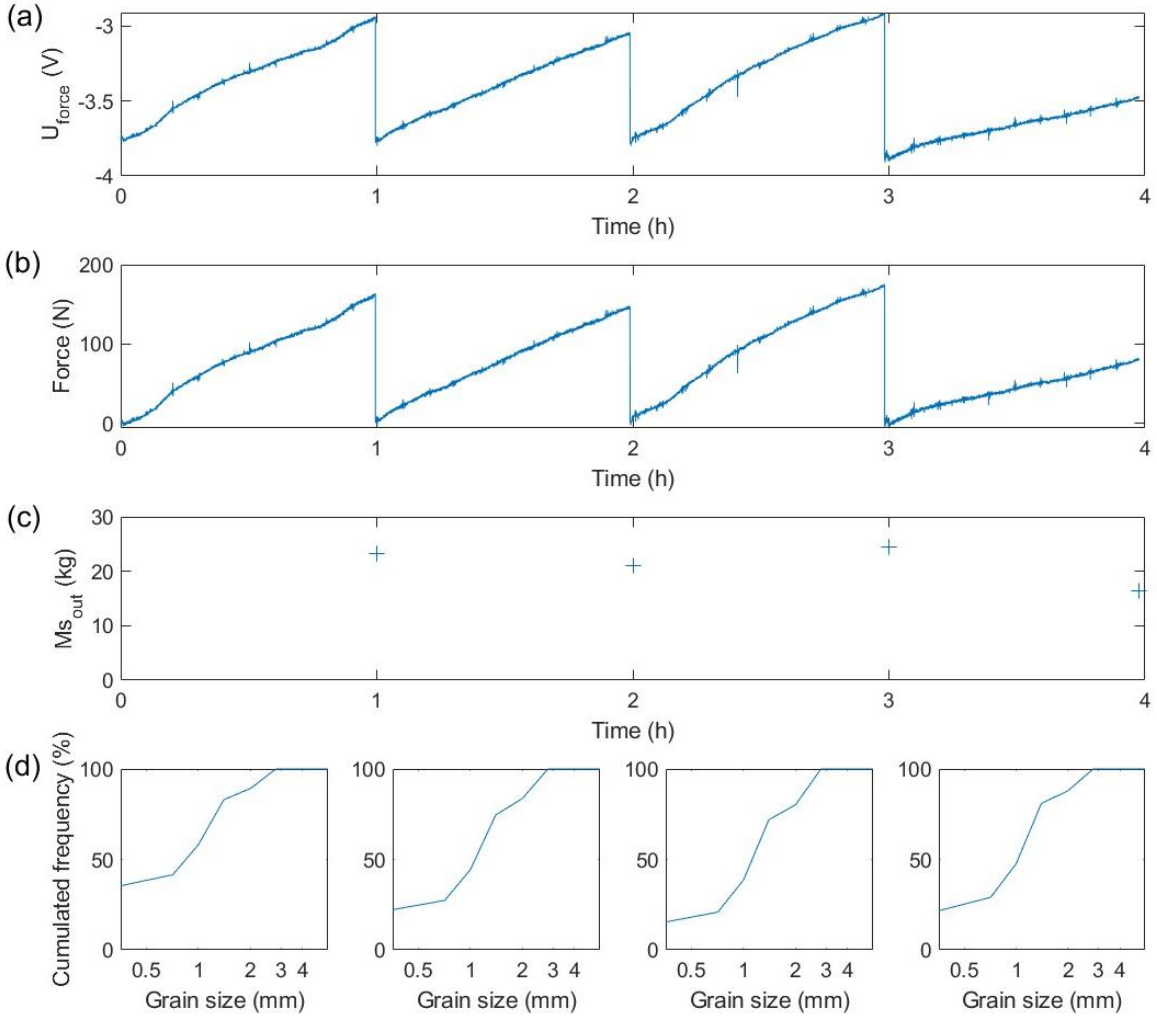

Figure 14: (a) Tension measured by the force sensor. (b) Converted tension in force. (b) Weighted mass at the end of each hour within the run. (d) Grain size distribution measured from the sediment output.

3.5.2. Potential treatment

These data can be used to estimate instantaneous sediment flux at the outlet using the force sensor and the weighted mass. The dataset gives the tension measured by the sensors that need to be converted to a force using equation 5.

https://doi.org/10.5194/essd-2026-197
Preprint. Discussion started: 25 June 2026

$$F_{sensor} = 200.U + 780 \quad \textbf{(5)}$$

Where F_{sensor} is the force measured by the sensor in N and U the tension in V.

As the tank is submerged, the force measured by the sensor comprises the tank weight and the Archimedes forces acting on the tank. Hence, the force related to sediment weight F_s is given in equation 6.

$$F_s = F_{sensor} - M_{tank}\mathrm{g} + \rho \mathrm{g} V_{tank} \quad \textbf{(6)}$$

Where M_{tank} is the mass of the tank in kg, g is the gravity in m.s^{-2}, ρ is the water density in kg/m^3 and V_{tank} is the submerged volume of the tank in m^3.

V_{tank} varies depending on the water level in the tank (due to the variation in discharge that is pumped in the outlet tank). However, due to the small proportion of volume that this variation represents, we choose to neglect the variation and use a constant value. We measure a value of 60.7 N for $M_{tank}\mathrm{g} + \rho \mathrm{g} V_{tank}$.

The output sediment mass could be analytically expressed, but because of many variations on the system, such as the water jet on the tank, we recommend to use the weighted mass to fit a coefficient between F_s and M_s. We also recommend to add an offset to force Fs to be equal to 0 at the beginning of each run stop, as shown in Figure 14b.

4. Potential data use

This dataset offers a wide range of applications in experimental and quantitative geomorphology. It enables the investigation of channel morphological responses to controlled boundary conditions, including variations in sediment supply, water discharge, and channel entrance constriction.

In a general perspective, several derived products can be generated from the raw data. These include, for example, Difference of DEMs (DoDs) to quantify spatial patterns of erosion and deposition, for geomorphological purposes (Figure 15c). It can also serve to estimate surface grain-size maps derived from roughness metrics (Figure 15a and b). Surface grain size can be estimated using the roughness-based method developed for braided rivers by Ribet et al. (2024), in which topographic roughness serves as a proxy for grain size. Calibration curves between roughness and sediment size can be established using homogeneous patches where grain size is measured either manually or via automated detection. Given the high precision of

https://doi.org/10.5194/essd-2026-197
Preprint. Discussion started: 25 June 2026

the DEMs, this approach enables robust spatial quantification of grain-size distribution and its temporal evolution, providing opportunities to investigate grain sorting processes and sedimentary feedback mechanisms.

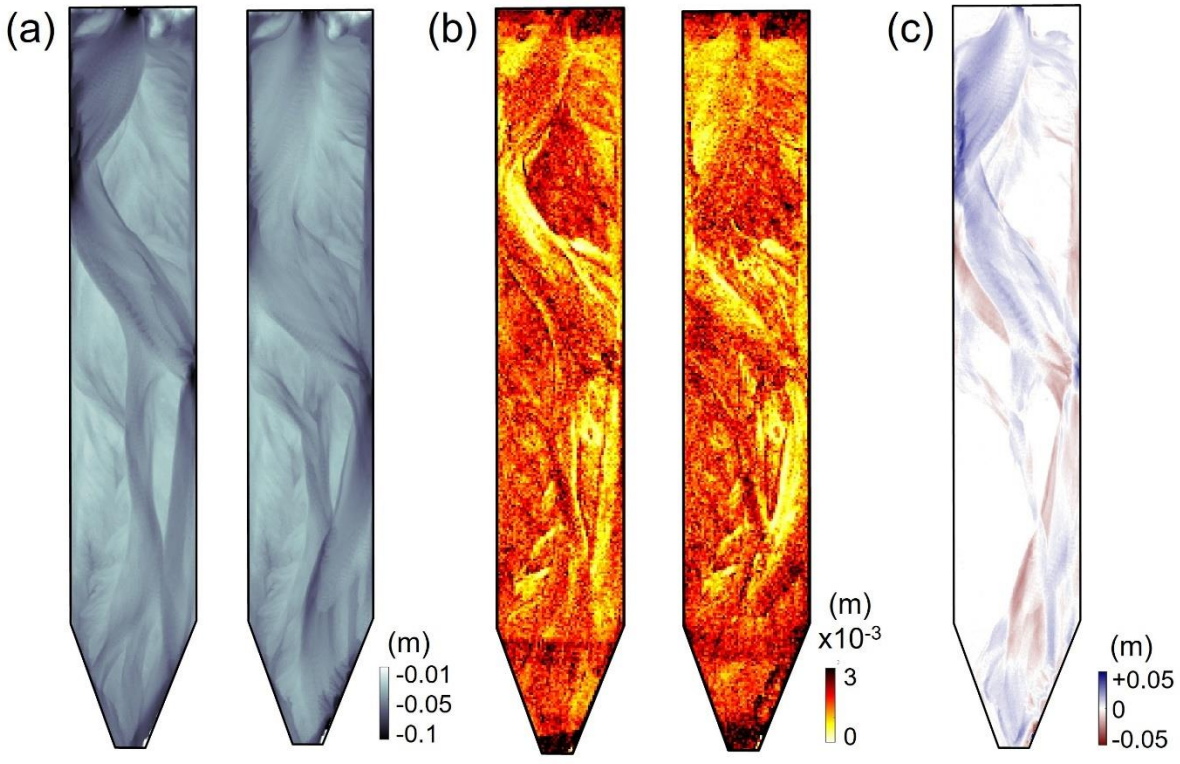

Figure 15: Example of data treatment. (a) shows two DEM before and after a large flood with the corresponding surface grain size map (b) and the difference of DEMs in (c).

The data combined with the presented derived results also offers a robust dataset to study numerical modelling issues. Among many other mathematical or numerical problems (Chavarrías et al., 2018; Tritthart et al., 2024), numerical modelling based on Saint Venant and Exner resolution equations do not fully account for all the physical processes that occur in complex gravel bed streams and are not robust in all hydraulics regime (Blom et al., 2008). The availability of high-resolution topographic data, flow velocities, and measured sediment outputs makes it possible to investigate those questions more precisely under controlled experimental conditions. Flow velocities are of interest to calibrate the model and many validation data are available depending on the question addressed. As an example, transported grain size and mobility issues can be addressed at a global

https://doi.org/10.5194/essd-2026-197
Preprint. Discussion started: 25 June 2026

scale using transported grain size measurement at the output and local surface grain sorting can be study using the surface grain sorting maps presented in Figure 15b. Erosion and deposition models can also be applied and DEMs as presented in Figure 15c can be used for comparison and validation.

In a more specific context of French alpine rivers, the data can be qualitatively used to understand the morphodynamics pattern related to the snow melt period and help to understand sediment transfer in gravel bed streams. This can be study through different morphological indicators such as the main slope, the Shields stress or with indicators dedicated to braided river such as the Bed Relief Index (BRI*) (Devreux et al., 2022; Liébault et al., 2013).

5. Conclusion

This paper presents a dataset collected during flume experiments designed to reproduce snowmelt flood events typical of alpine streams. Experiments were conducted under three different upstream configurations, each including several cycles composed of different flood types. The experimental design and instrumentation were developed so that the resulting data could be used both for general morphodynamic analyses and for numerical modeling purposes.

To this end, measurements include the evolution of bed topography, sediment transport rate at the outlet, grain-size distribution of transported material, and surface flow velocities. The dataset also contains timelapse videos of all experimental runs, recorded from different viewpoints. Considering the range of upstream configurations and hydrographs, the dataset can be used to investigate a variety of bedload and morphological processes across different spatial and temporal scales, including bedload estimation, the effects of sediment supply, grain sorting processes, and key controls on channel morphodynamics. It provides a large dataset comprising 115 DEMs, 35 videos for flow velocities estimates, 81 transported grain size distribution and videos for various input conditions.

Data availability

The dataset is available online at https://doi.org/10.57745/QM4ZOO (Johannot, 2026).

https://doi.org/10.5194/essd-2026-197
Preprint. Discussion started: 25 June 2026

Author contributions

AJ : Conceptualization, Data Curation, Formal Analysis, Methodology, Validation, Visualization, and Writing – original draft, review and editing.. AL and KB : Conceptualization, Methodology. AR : Supervision, Conceptualization and Writing – review and editing. HB, AB and FF : Methodology.

Competing interests

The authors declare that they don't have any conflict of interest.

Disclaimer

Copernicus Publications adds a standard disclaimer: "Copernicus Publications remains neutral with regard to jurisdictional claims made in the text, published maps, institutional affiliations, or any other geographical representation in this paper. While Copernicus Publications makes every effort to include appropriate place names, the final responsibility lies with the authors. Views expressed in the text are those of the authors and do not necessarily reflect the views of the publisher."
Please feel free to add disclaimer text at your choice, if applicable.

Review statement

The review statement will be added by Copernicus Publications listing the handling editor as well as all contributing referees according to their status anonymous or identified.

References

Ashmore, P. (1982). Laboratory modelling of gravel braided stream morphology. *Earth Surface Processes and Landforms*, *7*, 201–225.

Ashmore, P. E. (1988). Bed load transport in braided gravel-bed stream models. *Earth Surface Processes and Landforms*, *13*(8), 677–695. https://doi.org/10.1002/esp.3290130803

Ashmore, P., & Parker, G. (1983). Confluence scour in coarse braided streams. *Water Resources Research*, *19*(2), 392–402. https://doi.org/10.1029/WR019i002p00392

https://doi.org/10.5194/essd-2026-197
Preprint. Discussion started: 25 June 2026

Ashworth, P. J., Best, J., Leddy, J. O., & Geehan, G. W. (1994). The physical modelling of braided rivers and deposition of fine- grained sediment. *Process Models and Theoretical Geo-Morphology*, 115–139.

Bacchi, V., Recking, A., Eckert, N., Frey, P., Piton, G., & Naaim, M. (2014). The effects of kinetic sorting on sediment mobility on steep slopes. *Earth Surface Processes and Landforms*, *39*(8), 1075–1086. https://doi.org/10.1002/esp.3564

Bakker, M., Gimbert, F., Geay, T., Misset, C., Zanker, S., & Recking, A. (2020). Field Application and Validation of a Seismic Bedload Transport Model. *Journal of Geophysical Research: Earth Surface*, *125*(5). https://doi.org/10.1029/2019JF005416

Blom, A., Ribberink, J. S., & Parker, G. (2008). Vertical sorting and the morphodynamics of bed form-dominated rivers: A sorting evolution model. *Journal of Geophysical Research: Earth Surface*, *113*(F1), 2006JF000618. https://doi.org/10.1029/2006JF000618

Carbonari, C., Recking, A., & Solari, L. (2021). A simple image analysis technique for measuring bed surface texture in flume experiments. *Journal of Hydrology*, *598*, 126447. https://doi.org/10.1016/j.jhydrol.2021.126447

Carbonneau, P. E. (2005). The threshold effect of image resolution on image-based automated grain size mapping in fluvial environments. *Earth Surface Processes and Landforms*, *30*(13), 1687–1693. https://doi.org/10.1002/esp.1288

Carbonneau, P. E., Bergeron, N., & Lane, S. N. (2005). Automated grain size measurements from airborne remote sensing for long profile measurements of fluvial grain sizes. *Water Resources Research*, *41*(11). https://doi.org/10.1029/2005WR003994

Chavarrías, V., Stecca, G., & Blom, A. (2018). Ill-posedness in modeling mixed sediment river morphodynamics. *Advances in Water Resources*, *114*, 219–235. https://doi.org/10.1016/j.advwatres.2018.02.011

Deng, J., Brousse, G., & Jodeau, M. (2025). Gravel Replenishment Downstream of Dams: Insights From a Flume Experiment in a Straight Embanked Channel. *Water Resources Research*, *61*(6). https://doi.org/10.1029/2024wr037928

Devreux, L., Chapuis, M., & Belletti, B. (2022). Hydromorphological analysis on restored Alpine braided rivers. *Geomorphology*, *415*, 108404. https://doi.org/10.1016/j.geomorph.2022.108404

https://doi.org/10.5194/essd-2026-197
Preprint. Discussion started: 25 June 2026

Gilbert, G. K. (1914). *Transportation Of Debris By Running Water*. 265. US Government Printing Office.

Gomez, B. (1983). Temporal variations in bedload transport rates: The effect of progressive bed armouring. *Earth Surface Processes and Landforms*, *8*(1), 41–54. https://doi.org/10.1002/esp.3290080105

Hauet, A., Jodeau, M., Le Coz, J., Marchand, B., die Moran, A., Le Boursicaud, R., & Dramais, G. (2014). Application de la méthode LSPIV pour la mesure de champs de vitesse et de débits de crue sur modèle réduit et en rivière. *La Houille Blanche*, *100*(3), 16–22. https://doi.org/10.1051/lhb/2014024

Iseya, F., & Ikeda, H. (1987). Pulsations in Bedload Transport Rates Induced by a Longitudinal Sediment Sorting: A Flume Study Using Sand and Gravel Mixtures. *Geografiska Annaler*.

Jackson, W. L., & Beschta, R. L. (1982). A model of two-phase bedload transport in an oregon coast range stream. *Earth Surface Processes and Landforms*, *7*(6), 517–527. https://doi.org/10.1002/esp.3290070602

James, M. R., Chandler, J. H., Eltner, A., Fraser, C., Miller, P. E., Mills, J. P., Noble, T., Robson, S., & Lane, S. N. (2019). Guidelines on the use of structure-from-motion photogrammetry in geomorphic research. *Earth Surface Processes and Landforms*, *44*(10), 2081–2084. https://doi.org/10.1002/esp.4637

James, M. R., & Robson, S. (2014). Mitigating systematic error in topographic models derived from UAV and ground-based image networks. *Earth Surface Processes and Landforms*, *39*(10), 1413–1420. https://doi.org/10.1002/esp.3609

Johannot, A. (2026). *Experimental flume dataset on the morphological response of alpine gravel-bed rivers to flow and sediment forcing* [Data set]. Recherche Data Gouv. https://doi.org/10.57745/QM4ZOO

Kingsland, K. (2020). Comparative analysis of digital photogrammetry software for cultural heritage. *Digital Applications in Archaeology and Cultural Heritage*, *18*, e00157. https://doi.org/10.1016/j.daach.2020.e00157

Lane, S. N., Chandler, J. H., & Porfiri, K. (2001). Monitoring River Channel and Flume Surfaces with Digital Photogrammetry. *Journal of Hydraulic Engineering*, *127*(10), 871–877. https://doi.org/10.1061/(ASCE)0733-9429(2001)127:10(871)

Lane, S. N., James, T. D., & Crowell, M. D. (2000). Application of Digital Photogrammetry to Complex Topography for Geomorphological Research. *The Photogrammetric Record*, *16*(95), 793–821. https://doi.org/10.1111/0031-868X.00152

https://doi.org/10.5194/essd-2026-197
Preprint. Discussion started: 25 June 2026

Lane, S. N., Westaway, R. M., & Murray Hicks, D. (2003). Estimation of erosion and deposition volumes in a large, gravel-bed, braided river using synoptic remote sensing. *Earth Surface Processes and Landforms*, *28*(3), 249–271. https://doi.org/10.1002/esp.483

Leduc, P. (2013). *Etude expérimentale de la dynamique sédimentaire des rivières en tresses*. Université de Grenoble.

Liébault, F., Lallias-Tacon, S., Cassel, M., & Talaska, N. (2013). LONG PROFILE RESPONSES OF ALPINE BRAIDED RIVERS IN SE FRANCE. *River Research and Applications*, *29*(10), 1253–1266. https://doi.org/10.1002/rra.2615

Middleton, L. (2017). *Planform change and bedload transport in braiding rivers*. The University of Western Ontario.

Misset, C., Recking, A., Legout, C., Bakker, M., Bodereau, N., Borgniet, L., Cassel, M., Geay, T., Gimbert, F., Navratil, O., Piegay, H., Valsangkar, N., Cazilhac, M., Poirel, A., & Zanker, S. (2020). Combining multi-physical measurements to quantify bedload transport and morphodynamics interactions in an Alpine braiding river reach. *Geomorphology*, *351*, 106877. https://doi.org/10.1016/j.geomorph.2019.106877

Misset, C., Recking, A., Legout, C., Valsangkar, N., Bodereau, N., Zanker, S., Poirel, A., & Borgniet, L. (2019). The Dynamics of Suspended Sediment in a Typical Alpine Alluvial River Reach: Insight From a Seasonal Survey. *Water Resources Research*, *55*(12), Article 12. https://doi.org/10.1029/2019WR025222

Nasr, M., Johannot, A., Geay, T., Zanker, S., Le Guern, J., & Recking, A. (2023). Passive Acoustic Monitoring of Bed Load with Drifted Hydrophone. *Journal of Hydraulic Engineering*, *149*(7), 06023003. https://doi.org/10.1061/JHEND8.HYENG-13438

Over, J.-S. R., Ritchie, A. C., Kranenburg, C. J., Brown, J. A., Buscombe, D., Noble, T., Sherwood, C. R., Warrick, J. A., & Wernette, P. A. (2021). *Processing Coastal Imagery With Agisoft Metashape Professional Edition, Version 1.6-Structure From Motpn Workflow Documentation* (Open-File Report No. 1039). U.S. Geological Survey.

Parker, G., Dhamotharan, S., & Stefan, H. (1982). Model experiments on mobile, paved gravel bed streams. *Water Resources Research*, *18*(5), 1395–1408. https://doi.org/10.1029/WR018i005p01395

Parker, G., & Klingeman, P. C. (1982). On why gravel bed streams are paved. *Water Resources Research*, *18*(5), 1409–1423. https://doi.org/10.1029/WR018i005p01409

https://doi.org/10.5194/essd-2026-197
Preprint. Discussion started: 25 June 2026

Parker, G., Klingeman, P. C., & McLean, D. G. (1982). Bedload and Size Distribution in Paved Gravel-Bed Streams. *Journal of the Hydraulics Division*, *108*(4), 544–571. https://doi.org/10.1061/JYCEAJ.0005854

Peirce, S. E. K. (2017). *Morphological Bedload Transport in Gravel-Bed Braided Rivers*. The University of Western Ontario.

Piton, G., Recking, A., Le Coz, J., Bellot, H., Hauet, A., & Jodeau, M. (2018). Reconstructing Depth-Averaged Open-Channel Flows Using Image Velocimetry and Photogrammetry. *Water Resources Research*, *54*(6), 4164–4179. https://doi.org/10.1029/2017WR021314

Recking, A. (2006). *Etude expérimentale de l'influence du tri granulométrique sur le transport solide par charriage.* Institut National des Sciences Appliquées de Lyon.

Recking, A., Frey, P., Paquier, A., & Belleudy, P. (2009). An experimental investigation of mechanisms involved in bed load sheet production and migration. *Journal of Geophysical Research: Earth Surface*, *114*(F3), 2008JF000990. https://doi.org/10.1029/2008JF000990

Recking, A., Johannot, A., Horita, K., Nasr, M., Vázquez-Tarrío, D., Zanker, S., Fontaine, F., & Melun, G. (2024). An Attempt to Take Into Account Natural Variability in 1D Bedload Prediction. *Journal of Geophysical Research: Earth Surface*, *129*(7), e2023JF007601. https://doi.org/10.1029/2023JF007601

Ribet, L., Liébault, F., Borgniet, L., Deschâtres, M., & Melun, G. (2024). *Surface grain-size mapping of braided channels from SfM photogrammetry*. https://doi.org/10.5194/egusphere-2024-3697

Tritthart, M., Vanzo, D., Chavarrías, V., Siviglia, A., Sloff, K., & Mosselman, E. (2024). Why do published models for fluvial and estuarine morphodynamics use unrealistic representations of the effects of transverse bed slopes? *Advances in Water Resources*, *193*, 104831. https://doi.org/10.1016/j.advwatres.2024.104831

Vesipa, R., Camporeale, C., & Ridolfi, L. (2017). Effect of sampling time in the laboratory investigation of braided rivers. *Water Resources Research*, *53*(6), 5184–5197. https://doi.org/10.1002/2017WR020474

Williams, R. D., Brasington, J., & Hicks, D. M. (2016). Numerical Modelling of Braided River Morphodynamics: Review and Future Challenges. *Geography Compass*, *10*(3), 102–127. https://doi.org/10.1111/gec3.12260